^{99m}Tc-MIBI than ^{131}I shown in the present study agress with previous observations by Sundram et al. (*14*) and may also reflect the nonfunctioning nature of the tumors.

CONCLUSION

Although we did not perform a prospective study to evaluate whether ^{99m}Tc-MIBI is useful for early detection of tumor recurrence, the sensitivity of this technique for the detection of metastases warrants its use for clinical follow-up of postoperative patients with thyroid carcinoma. Finally, ^{99m}Tc-MIBI is advantageous over ^{201}Tl, because it detects metastatic lesions.

ACKNOWLEDGMENTS

We thank Miss Yukiko Mieda for administrative assistance and Miss Katsuko Nakagawa and Mr. Toru Fujita for technical assistance.

REFERENCES

1. Van Herle AJ, Uller RP. Elevated serum thyroglobulin: a marker of metastases in differentiated thyroid carcinomas. *J Clin Invest* 1975;56:272–275.
2. Ramanna L, Waxman A, Brachman M, et al. Correlation of thyroglobulin measurements and radioiodine scans in the follow-up of patients with differentiated thyroid cancer. *Cancer* 1985;55:1525–1529.
3. Iida Y, Hidaka A, Hatabu H, Kasagi K, Konishi J. Follow-up study of postoperative patients with thyroid cancer by thallium-201 scintigraphy and serum thyroglobulin measurement. *J Nucl Med* 1991;32:2098–2100.
4. Tonami N, Hisada K. Thallium-201 scintigraphy in postoperative detection of thyroid cancer: a comparative study with ^{131}I. *Radiology* 1980;136:461–464.
5. Hoefnagel CA, Delprat CC, Marcuse HR, de Vijlder JJM. Role of thallium-201 total-body scintigraphy in follow-up of thyroid carcinoma. *J Nucl Med* 1986;27:1854–1857.
6. Hassan IM, Sahweil A, Constantinides C, et al. Uptake and kinetics of ^{99m}Tc-hexakis-2-methoxyisobutylisonitrile in benign and malignant lesions in the lungs. *Clin Nucl Med* 1989;14:333–340.
7. Caner B, Kitapcl M, Unlu M, et al. Technetium-99m-MIBI uptake in benign and malignant bone lesions: a comparative study with technetium-99m-MDP. *J Nucl Med* 1992;33:319–324.
8. Aktolun C, Bayhan H, Kir M. Clinical experience with ^{99m}Tc-MIBI imaging in patients with malignant tumors. Preliminary results and comparison with ^{201}Tl. *Clin Nucl Med* 1992;17:171–176.
9. Kao CH, Wang SJ, Liao SQ, Lin WY, Hsu CY. Quick diagnosis of hyperthyroidism with semiquantitative 30-min ^{99m}Tc-MIBI thyroid uptake. *J Nucl Med* 1993;34:71–74.
10. Scott AM, Kostakoglu L, O'Brien JP, Straus DJ, Abdel-Dayem HM, Larson SM. Comparison of technetium-99m-MIBI and thallium-201-chloride uptake in primary thyroid lymphoma. *J Nucl Med* 1992;33:1396–1398.
11. Földes I, Levay A, Stotz G. Comparative scanning of thyroid nodules with ^{99m}Tc-pertechnetate and ^{99m}Tc-MIBI. *Eur J Nucl Med* 1993;20:330–333.
12. Yen TC, Lin HD, Lee CH, Chang SL, Yeh SH. The role of technetium-99m-sestamibi whole-body scans in diagnosing metastatic Hürthle cell carcinoma of the thyroid gland after total thyroidectomy: a comparison with iodine-131 and thallium-201 whole-body scans. *Eur J Nucl Med* 1994;21:980–983.
13. Lebouthillier G, Morais J, Picard M, Picard D, Chartrand R, D'Amour P. Technetium-99m-sestamibi and other agents in the detection of metastatic medullary carcinoma of the thyroid. *Clin Nucl Med* 1993;18:657–661.
14. Sundram FX, Goh ASW, Ang ES. Role of technetium-99m-sestamibi in localization of thyroid cancer metastases. *Ann Acad Med Singapore* 1993;22:557–559.
15. Nemec J, Nyvltova O, Blazek T, et al. Positive thyroid cancer scintigraphy using technetium-99m-methoxyisobutylisonitrile. *Eur J Nucl Med* 1996;23:69–71.
16. Dadparvar S, Chevres A, Tulchinsky M, Krishna-Badrinath L, Khan AS, Slizofski WJ. Clinical utility of ^{99m}Tc-MIBI imaging in differentiated thyroid carcinoma: comparison with ^{201}Tl and ^{131}I Na scintigraphy and serum thyroglobulin quantitation. *Eur J Nucl Med* 1995;22:1330–1338.
17. Mueller SP, Piotrowski B, Guth-Tougelides B, Reiners C. Technetium-99m-MIBI and ^{201}Tl uptake in thyroid carcinoma [Abstract]. *J Nucl Med* 1988;29(suppl):854.
18. Baillet GY, Mena IG, Kuperus JH, Robertson JM, French WJ. Simultaneous technetium-99m-MIBI angiography and myocardial perfusion imaging. *J Nucl Med* 1989;30:38–44.
19. Strauss H, Pitt B. Thallium-201 as a myocardial imaging agent. *Semin Nucl Med* 1977;7:49–58.
20. Kao CH, Wang SJ, Lin WY, Hsu CY, Liao SQ, Yeh SH. Differentiation of single solid lesions in the lungs by means of SPECT with ^{99m}Tc-MIBI. *Eur J Nucl Med* 1993;20:249–254.
21. Chiu ML, Kronauge JF, Piwnica WD. Effect of mitochondrial and plasma membrane potentials on accumulation of hexakis (2-methoxyisobutylisonitrile) technetium(I) in cultured mouse fibroblasts. *J Nucl Med* 1990;31:1646–1653.
22. Rao V, Chiu M, Kronauge J, Piwnica-Worms D. Expression of recombinant human multidrug resistance P-Glycoprotein in insect cells confers decreased accumulation of ^{99m}Tc-sestamibi. *J Nucl Med* 1994;35:510–515.
23. Datz FL. Diffuse pulmonary uptake. In: *Gamuts in nuclear medicine*, 3rd ed. St. Louis, MO: Mosby Year Book Inc; 1995;382–383.
24. Miller DD, Heyl BL, Walsh RA. Lung uptake of technetium-99m hexamibi isonitrile during acute reversible ischemic left ventricular dysfunction in conscious dogs. *Circulation* 1988;78:(suppl):II-387.

Tumor Quantitation and Monitoring in Whole-Body Planar Technetium-99m-Sestamibi Imaging

Serge D. Van Kriekinge, Guido Germano, Charles Forscher, Gerald Rosen, Pawan Gupta and Alan D. Waxman

Department of Medical Physics and Imaging and Division of Nuclear Medicine, Department of Imaging, The Burns and Allen Research Institute, Cedars-Sinai Medical Center; The Cedars-Sinai Comprehensive Cancer Center; Department of Radiological Sciences, UCLA School of Medicine; Los Angeles, California

We have developed a completely automatic software package to normalize, rigidly register and elastically match serial whole-body planar images from patients with limb tumors. Variations in tumor uptake and size are analyzed and quantitated by the software. **Methods:** The software consists of a chain of modules incorporating several automatic algorithms. A rigid registration algorithm aligns images by translation and rotation based on feature points corresponding to the patient's neck and bladder. An elastic matching algorithm generates a grid for each image in a sequence by combining thresholding and local feature analysis in the head, torso and leg regions. A linear warping algorithm then interpolates pixel values and locations to make the grid points in all images coincide with the grid points of one of them (the reference image). All images in a sequence are normalized based on brain uptake. Quantitation of tumor uptake and size is performed in all images using an ROI automatically determined from a single user-selected seed point. **Results:** The software was tested on four 2-image and one 3-image sequences from five patients (11 images). Quantitative measurements of body contour overlap show an average intrasequence agreement of 73.4%, 78.7% and 91.5% for unregistered, rigidly registered and rigidly registered + matched images, respectively. **Conclusion:** Our method represents an objective, quantitative tool to measure tumor activity in sequential whole-body scintigraphic images, and may help assess tumor response to chemotherapy or radiation therapy.

Key Words: tumor quantitation; whole-body image registration; planar scintigraphy image registration

J Nucl Med 1997; 38:356–361

The comparison of whole-body planar scintigraphic images recorded sequentially in conjunction with chemotherapy or radiation therapy is an important tool in assessing the effectiveness of a treatment. Technetium-99m-sestamibi and ^{201}Tl have been used frequently to detect and evaluate primary and metastatic tumors (*1–8*). Changes in the tumor size or uptake between serial images are currently assessed subjectively

Received March 25, 1996; revision accepted July 1, 1996.

For correspondence or reprints contact: Guido Germano, PhD, Director, Nuclear Medicine Physics, Cedars-Sinai Medical Center A047 N, 8700 Beverly Blvd., Los Angeles, CA 90048.

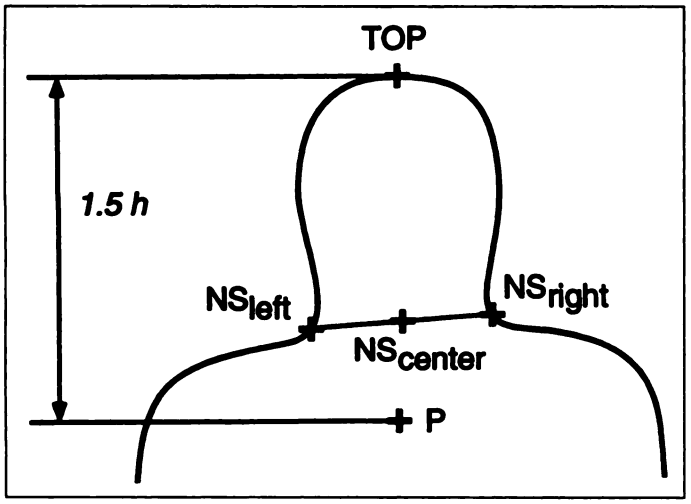

FIGURE 1. Location of the neck-shoulders points NS_{left}, NS_{right} and their middlepoint NS_{center}.

through visual interpretation. Assessment of sequential images can be made more accurate at times using a multistep gray or color scale to display the images. However, inappropriate intensity settings and variable uptake in areas other than the tumor site (i.e., gastrointestinal tract, bladder) cause a visual approach alone to be difficult or misleading, especially in assessing tumor response to therapy.

The current study describes a software system that automatically registers two or more whole-body planar images based on anatomical features. After the visual identification of the tumor in one of the images and manual marking of a pixel inside it, the software automatically quantitates the tumor's size and uptake in all images, normalizes it to brain uptake and outputs a quantitative measurement of its evolution during therapy.

The software algorithms use the techniques of morphological filtering (*9*) and warping (*10*) to achieve their goals of rigid-body registration, elastic matching and differential analysis. Some of these techniques have previously been used for medical image registration and atlas generation, in particular for brain MRI, CT, PET and SPECT images (*11–13*). Other techniques were successfully applied to register three-dimensional brain images (e.g., iterative registration based on the sum of absolute difference (*14*), principal axes transformation (*15*)), or thoracic images (least-squares fitting of surfaces (*16*)), but not whole-body images. Planar whole-body images are particularly well-suited to the assessment of tumors of the extremities, since a reference site within the body that may be distant from the tumor can be selected for purposes of normalization. In addition, whole-body surveys offer the opportunity to detect additional tumor sites distant from the primary site. Extremity tumors, especially sarcomas, represent the main focus of this study. Of course, limbs are especially likely to be bent or rotated in different ways from study to study, making it virtually impossible to achieve registration of even same-patient whole-body images by the rigid-body approach alone. Hence, the need for a composite strategy that combines rigid-body registration with elastic matching, as presented in this paper.

MATERIALS AND METHODS

General Structure of the Software

The software applies a sequence of processing operations to two or more images. These operations are: automatic cropping, rigid-body registration, normalization, elastic matching and differential analysis. Elastic matching and differential analysis will only yield meaningful results if applied to images of the same patient. The processing sequence can be executed automatically (all operations are applied successively to the images), or manually (the user selects a particular operation to be applied to specific images). Each processing operation generates a new set of images, thus preserving all intermediate results: in case of failure of one of the algorithms, the user can modify some parameters and either restart the automatic processing or select the operations to be performed manually. All the thresholds used are expressed as a percentage of the maximum pixel value in the image being processed, and can be modified by the user.

All software was written in C++ and compiled with the GNU G++ compiler on a Sun Sparcstation 20 running under the SunOS 4.2 operating system (Sun Microsystems, Mountain View, CA). The user interface was implemented with the X-Windows Motif library (The Santa Cruz Operation, Santa Cruz, CA). Execution time for the complete processing sequence (from automatic cropping to differential analysis) totaled 2 min per image. The application interfaces with the clinical database access software in use at the Division of Nuclear Medicine of Cedars-Sinai Medical Center.

Automatic Cropping

Before processing begins, all the images are cropped to reduce disk storage space and memory requirements. Cropping is performed automatically by searching for the bounding box of pixels with a value above a predefined threshold (initially 0.5%). Typically, an image I_o has an initial size of 512 × 1024 pixels, which is decreased to about 300 × 600 pixels for its cropped version I_c, a threefold reduction (see Appendix for image-naming conventions).

Rigid-Body Registration

The purpose of this operation is to realign the torso of the patient across images. This is done by detecting three feature points: two points at the neck-shoulders junctions, and the centroid of the bladder.

First, a convolution with a 5 × 5 blurring kernel is performed on every cropped image, with the goal of reducing the influence of local variations without removing important features from the image. The image is then binarized (using a 1% threshold), and the resulting image is morphologically eroded twice with a 5 × 5 pseudocircular structuring element (*9*) to generate image I_e. Morphological erosion removes pixels at the periphery of objects in a binary image, the thickness of the layer depending on the structuring element that serves as a mask. This step serves to eliminate artifacts due to external activity sources (e.g., isotope left in the injection line when the latter cannot be positioned outside of the camera's field of view). The second purpose of the erosion is to eliminate the relatively hot layer of pixels corresponding to the scalp, calvaria and head muscles to ensure accurate image normalization later on. The structuring element chosen for this study removes 10 pixels when used twice, approximately 35 mm. The bounding box of the binary image is determined and measured, providing an estimate b of the patient's body length. That estimate is used to determine approximate dimensions for various body structures, such as the head (head height: h = b/8) and the legs (leg length: l = b/3, to ensure we do not include the pelvic area).

A closed contour of the patient's body is then generated by an additional morphological erosion of I_e and a subtraction of this further eroded image from image I_e. The neck-shoulders junction points are located by a radial search from a point P located at 1.5*h from the top of the head (TOP) (Fig. 1). The closest point to the search center on each side is kept as junction point (NS_{left} and NS_{right}). Let NS_{center} be the midpoint of the NS_{left}—NS_{right} segment.

It is assumed that the bladder is the brightest structure in the central pelvic area. The search for a pixel brighter than 90% of the maximum pixel count is conducted starting at the lower third of the image (approximately midthigh) and going upward (i.e., decrementing the *y* coordinate). For each line a 100-pixel wide horizontal segment (approximately 35 cm) is analyzed, with the pixels

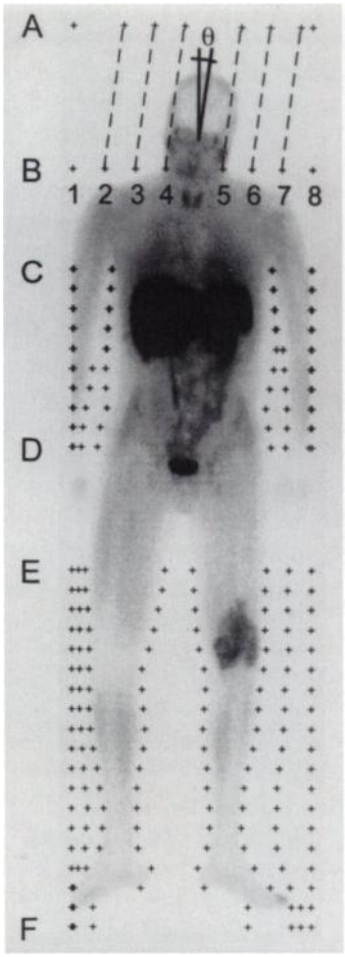

FIGURE 2. Elastic matching grid generation for a typical whole-body scan. Row A is located at the top edge of the image. Row B is at the y coordinate of NS_{center}. Points 4 and 5 on row B are determined using the x coordinates of NS_{left} and NS_{right}. Points 2 and 3 are interpolated between 1 and 4, and 6 and 7 are interpolated between 5 and 8. The grid points on row A are derived from those on row B using the head tilt angle θ. Rows C through D are determined using the torso-specific algorithm, and rows E through F using the legs-specific algorithm.

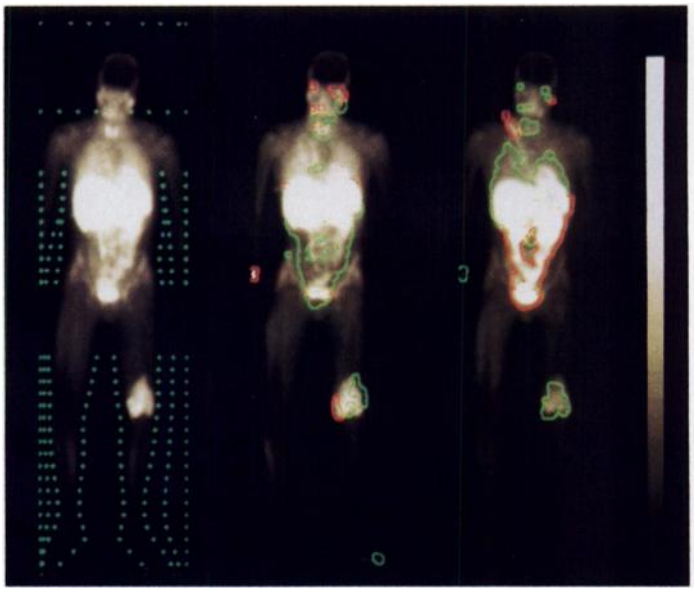

FIGURE 3. Automatically-registered and elastically-matched sequential images of a 21-yr-old man with osteosarcoma (5a in Table 1). Grid points used for matching are shown as green crosses in the reference image (left), while areas of increased (red) and decreased (green) uptake in later images (center and right) help identify potential tumor sites.

closest to the center of the segment being examined first. If no pixel is found that meets the 90% requirement, the search algorithm selects the next line. Once such a pixel is found, the local maximum in a 15 × 15-pixel square region surrounding the pixel is located and the centroid of the 10 × 10-pixel square region that surrounds this local maximum is computed. The centroid represents the location of the bladder (BL).

One of the images to be registered is selected as reference and will not be modified. All other images are translated to make their NS_{center} point coincide with that of the reference, then rotated to align all torsos (NS_{center}—BL segments). I_r^0 is therefore identical to I_c^0 and I_r^1 is the registered version of I_c^1 (see Appendix for superscript convention).

Normalization and Head Tilt Angle

Using the eroded binary image I_e as a mask, an estimate of the average brain uptake (u) is computed by averaging pixel counts in the upper half of the head (corresponding to the upper half of the NS_{center}—TOP segment in Fig. 1) for all the cropped images. For example, the pixel values for a reference image I_n^0 and a later image I_n^1 would be:

$$I_n^0(x, y) = I_r^0(x, y) \cdot \frac{u_{max}}{u^0} \qquad \text{Eq. 1}$$

$$I_n^1(x, y) = I_r^1(x, y) \cdot \frac{u_{max}}{u^1} \qquad \text{Eq. 2}$$

where u^0 and u^1 represent the average brain uptake in I_c^0 in and I_c^1, respectively, and $u_{max} = \max(u^0, u^1)$, such that the images are normalized to the highest average brain uptake.

Another characteristic parameter, the tilt angle of the head θ with respect to the y direction (patient axis), is computed using the eroded image. First, the middle point of each horizontal segment making up the head is selected. Then, those points are fitted to a straight line, and the tilt angle θ is derived from the slope of that line (Fig. 2).

Elastic Matching

Rigid registration of the images achieves alignment of the torso. However, the head may be slightly tilted or rotated, and the limbs may be in a different position between successive acquisitions. These factors require the additional processing step of elastic matching to better correlate the images.

Elastic matching is performed by generating a grid for each image in the sequence, then interpolating image pixel coordinates and values to make all grids coincide with that selected as the reference grid. Each grid can be divided in three regions corresponding to the patient's head, torso and legs.

The head region only contains two rows of eight points each generated from the neck points (NS_{left} and NS_{right}) and the head tilt angle (θ), as shown in Figure 2. In the torso region, eight points are identified on pixel rows selected using a constant spacing s (s = 10 by default). Two points correspond to the edges of the image, two define the boundaries of the abdomen, and four define the boundaries of the arms.

In the leg region, six points are detected every s^{th} pixel row: two at the edges of the image and four at the boundaries of the legs.

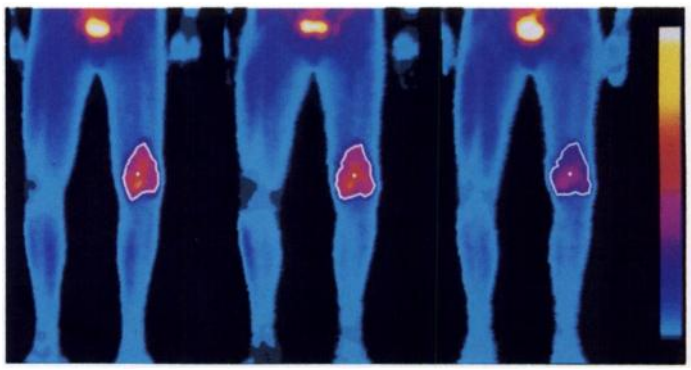

FIGURE 4. Tumor ROIs automatically computed from three sequential registered and elastically matched images of the patient in Figure 3.

Two additional points are inserted to ensure the uniformity of the grid (Fig. 2).

Point identification is based on global thresholding (default level = 2%). If more or less than eight or six points are detected for the torso and the legs, respectively, the algorithm adds or rejects points based on continuity rules with adjacent grid rows. As shown in Figure 2, two regions do not contain grid points: the shoulders and the pelvic area. The absence of grid points between the lower row of the head region and the upper row of the torso region, and between the lower row of the torso and the upper row of the leg region ensures a smooth transition between areas where different selection methods for the grid points are used.

Each grid defines a quadrangular mesh. Once the grids for the reference image I_n^0 and later image I_n^1 have been computed, a new, matched image I_m^1 is generated. The value of each pixel in I_m^1 is the value of the corresponding pixel in I_n^1, the location of this homologous pixel being determined by linear interpolation between grid points. This method is part of the local projective coordinate transformations category described by van den Elsen et al. (*17*).

Differential Analysis

This analysis is performed on the matched images. First, the difference between the reference and the later image is computed:

$$\Delta I(x, y) = I_m^1(x, y) - I_m^0(x, y) \qquad \text{for every } (x, y). \quad \text{Eq. 3}$$

The minimum and maximum pixel values in ΔI are extracted:

$$\min_{\Delta I} = \max(\Delta I(x, y)) \qquad \text{Eq. 4}$$

and

$$\max_{\Delta I} = \max(\Delta I(x, y)) \qquad \text{Eq. 5}$$

and ΔI is modified by remapping pixel values to one of the following values:

1 if $\Delta I(x, y) \leq k \cdot \min_{\Delta I} < 0$

0 if $\Delta I(x, y) > k \cdot \min_{\Delta I}$ and $\Delta I(x, y) < k \cdot \max_{\Delta I}$

2 if $\Delta I(x, y) \geq k \cdot \max_{\Delta I} > 0$,

where k is the differential analysis threshold (10% by default).

Then, we apply the morphological dilation operator to ΔI using a 5 × 5 pseudocircular structuring element (*9*) and subtract the resulting image from ΔI to obtain a double contour image I_d comprised of pixels with values −1, 0 or 1. Using I_m^1 and I_d, a composite image is generated that overlays I_m^1 with green contours around regions of decreased activity and red contours around regions of increased activity (Fig. 3).

The differential analysis is meant to assist the user in detecting areas that might be of interest to perform a quantitative analysis. The sensitivity of the algorithm can be modified by varying the value of k.

Tumor Quantitation

After visual identification of the tumor on the matched reference image I_m^0 or the matched later image I_m^1, and manual marking of a pixel (seed point) inside the tumor, a search for the local maximum is performed, and the tumor centroid is computed for a 10 × 10-pixel window around that point. The algorithm searches for the pixel value closest to the threshold value along each of 20 equally spaced radii originating from this centroid and spanning a complete 360° circle. Figure 4 shows the closed contours obtained when joining these pixels.

Since I_m^0 and I_m^1 have been matched, the seed point need only be selected on one image. The chosen image should be the one where the tumor is most visible. The software automatically computes ROIs outlining the tumor in both matched images proceeding from the same seed point, although the user can elect to copy the ROI computed on one image to the other image, or manually edit the contours on both images.

The algorithm outputs the following information for each image: tumor size in pixels, total and average tumor activity normalized to the brain activity u_{max}, and relative difference between tumor activity in I_m^0 and I_m^1:

$$\delta \text{ act} = \frac{\text{act } (I_m^1) - \text{act } (I_m^0)}{\text{act } (I_m^0)} \qquad \text{Eq. 6}$$

where act (I) is the total activity of the tumor in image I.

TABLE 1
Percent Overlap in Pairs of Cropped, Registered and Final Images

Patient no.	m_c [%]*	m_r [%]†	m_m [%]‡
1	81.5	82.5	89.6
2	68.6	79.3	88.8
3	69.4	73.0	93.5
4	74.0	83.5	92.6
5a	77.3	78.3	92.0
5b	69.6	75.3	92.4
Average	73.4	78.7	91.5
s.d.	5.2	4.0	1.8

*Cropped images.
†Registered images.
‡Registered and matched images.

Patient Studies

The registration and analysis algorithms were tested on 11 image sets collected from five patients between January 26 and July 7, 1995. Four patients had two studies and one patient had three studies, for a total of 11 image sets or 22 images (anterior + posterior views). The average interval between acquisitions was 52 ± 17 days (range = 36–80). Only the 11 anterior images are considered for the purposes of our study, since application of the algorithms to the posterior images yielded similar results.

Whole-body studies were performed after the intravenous injection of 30 mCi of ^{99m}Tc-sestamibi. Images began 10 min after injection. All patients were scanned using a 180° dual detector whole-body imager Genesys camera (ADAC Laboratories, Milpitas, CA) at a scan speed of 10 cm/min. Acquisition time was approximately 30 min per patient.

TABLE 2
Absolute Difference between Cropped, Registered and Final Images

Patient no.	d_c [%]*	d_r [%]†	d_m [%]‡
1	35.2	46.5	43.3
2	32.8	24.0	19.9
3	38.9	29.1	23.3
4	43.2	36.5	32.1
5a	21.8	23.2	14.6
5b	33.6	27.1	19.8
Average	34.3	31.1	25.5
s.d.	7.2	8.9	10.4

*Cropped images.
†Registered images.
‡Registered + matched images.
All numbers are shown as percentages of the average count value of the first image in each pair.

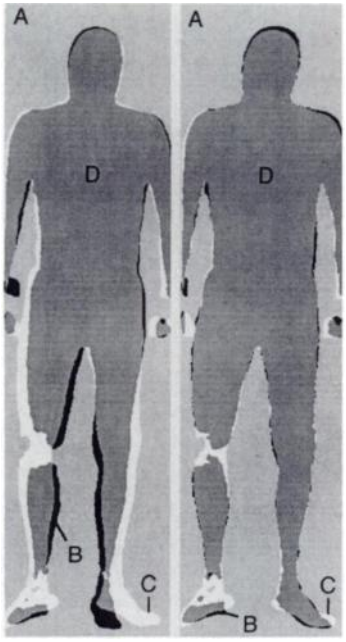

FIGURE 5. Superimposition of a pair of reference/later-registered images (left) and reference/later-matched images (right) for the patient in Figures 3 and 4.

Improvement Assessment

To quantify the improvement produced by the use of combined rigid registration and matching over rigid registration alone, we compared for each patient the reference and later image at the cropped, registered and matched level. All comparisons were performed by measuring the agreement (Method 1) or the difference (Method 2) between images I_c^0 and I_c^1, between I_r^0 and I_r^1, and between I_m^0 and I_m^1. For one of the patients, three sets of images were available and the comparison was performed between I^0 and I^1 (reported as 5a in Tables 1 and 2), and between I^0 and I^2 (reported as 5b in Tables 1 and 2).

Method 1. The reference and later image are binarized, and the number of pixels in each of four regions is computed. The four regions are the background pixels (A), pixels that belong to the body in the reference image only (B), pixels that belong to the body in the later image only (C), and pixels that belong to the body in both the reference and the later images (D) (Fig. 5). A perfect match would result in # pixels in B = # pixels in C = 0. A measure of the image agreement can be computed as:

$$m = \frac{\#\text{ pixels in D}}{\#\text{ pixels in (B + C + D)}}. \qquad \text{Eq. 7}$$

If m = 0, there is no overlap between the patient's body position in the two images, while m = 100% if there is perfect overlapping.

Method 2. The sum of the absolute differences between pixel count values in an image pair is computed and divided by the total count value in the reference image of that pair (this is equivalent to computing the ratio of average values, since the total number of pixels remains constant):

$$d = \frac{\sum_{x,y} |I^1(x, y) - I^0(x, y)|}{\sum_{x,y} I^0(x, y)}. \qquad \text{Eq. 8}$$

If the agreement were perfect, this difference would be equal to 0. In practice, due to Poisson statistics, inaccuracies of the algorithms, and differences in relative uptake between images, the average absolute difference will always be greater than zero, a lower value representing a better agreement.

RESULTS

Registration Versus Matching

With the set of default threshold values, visual inspection demonstrated that the automatic processing provided correct registration and elastic matching for all five patients. One matched image suffered from an apparent slight distortion at the ankles because of low counts that prevented a complete grid generation at the patient's feet level. Overall, the test datasets presented a wide range of challenges for an automatic processing algorithm: presence of extracorporeal residual activity sources, large head and feet rotation between successive images, limbs positioned partially outside the field of view of the camera, one amputated limb.

Image comparison Methods 1 and 2 were applied to three pairs of images for Patients 1 through 4 (six pairs for Patient 5), and the agreement parameters m and d were measured and compared. Table 1 shows that, based on Method 1, overall image agreement improved from 73.4% (no processing) to 78.7% (rigid registration alone) to 91.5% (rigid registration + elastic matching). Similarly, Table 2 shows that, based on Method 2, the difference between images decreases from 34.3% (no processing) to 31.1% (rigid registration alone) to 25.5% (rigid registration + elastic matching).

DISCUSSION

Landmark Points

The neck-shoulders points and the bladder were chosen because they can be consistently found across images: the neck-shoulders points are determined by a robust contour analysis procedure, and the bladder always appears as a bright structure since sestamibi is excreted in urine.

The neck-shoulders points are used for the translational component of the rigid registration algorithm because their position is more reliable than the bladder's. As to the rotational component, only the x coordinate of the bladder is really significant since the NS_{center}—BL segment is approximately vertical. In this regard, even if the bladder is differently filled in the various images, its symmetrical expansion perpendicularly to the patient's axis does not significantly change the x coordinate of its centroid.

Reference Activity

Our choice of using the brain for count normalization purposes is based on the documented low uptake of sestamibi in the brain in the absence of pathologies (*19,20*). Previous quantitation methods have used cardiac activity as reference (*21*), but in whole-body planar images, the heart is difficult to locate automatically due to its relatively small size and the presence of overlapping structures. In addition, cardiac activity may vary relative to other body structures due to physiologic variability in the excretion of pharmaceuticals such as sestamibi, as well as to differential washout rates. Other possible normalization choices include tumor-adjacent or contralateral normal tissue (*22*), but in our analysis such reference regions could not be consistently determined using an automatic approach.

Elastic Matching Features

It is important to select the grid points in such a way that elastic matching of the limbs can be performed without dramatically altering anatomical proportions. For example, choosing to identify a leg's axis instead of its boundaries could result in its artifactual thickening or thinning. A possible alternative to our approach would be to modify the radial function-based method described in Arad and Reisfeld (*23*) to use nonisotropic functions reflecting the oblong limb shape.

Another decision concerns the spacing of the elastic matching

grid. Larger vertical sampling yields a smoother image but can miss image detail. We chose a sampling interval of 10 pixels (approximately 35 mm), empirically determined to offer the best trade-off between image resolution and uniformity.

Elastic Matching Algorithm

The current software implementation uses linear interpolation for the location of a point within a grid quadrangle. This approach is adequate for dense grids, but may introduce discontinuity artifacts on pixel rows that correspond to grid rows (*18*), especially if the vertical sampling interval is large. A possible solution to this problem would be the use of a thin-plate spline or a Gaussian deformation model (*24*), although the computational complexity of these strategies could have a severely negative impact on software execution time.

Performance of the Matching Algorithm

Tables 1 and 2 show that the agreement is virtually always improved by the matching algorithm, regardless of the quantification method used. The only exception to this finding, for Patient 1 with Method 2, can be seen by visual inspection to be due to large perfusion differences in the patient's arms and legs between images, possibly due to physical exertion. Since Method 1 uses binarized images, it is not affected by this or similar problems.

We note that the threshold used to binarize the images in Method 1 may influence the results obtained. A higher threshold will remove most of the background noise from the analysis, and may also eliminate the low activity areas in the image, which are often the ones that might cause problems in the matching algorithm.

Comparison of the performance of the algorithms described in this paper with other registration techniques is problematic, because published methods deal only with individual, nonarticulated structures such as the brain (*11–15*), the heart (*14*), the liver (*14*) or the thorax (*16*). Moreover, validation often uses simulated rigid translation and rotation of the same image set (*11,14,15*), a situation intrinsically more favorable than comparison of sequential image sets. With that in mind, reported accuracies for published registration methods are in the few millimeters range for translations, and a few degrees range for rotations. An analogous parameter, the average absolute distance between external contours of registered and matched images, is 1.88 ± 0.53 pixels or 6.58 ± 1.85 mm with our method, as determined from the six pairs of final superimposed images.

Further Developments

Although our study was conducted using sestamibi as the imaging agent, we believe there is potential for application to other types of whole-body scans including ^{67}Ga-citrate, octreotide, other peptide and antibody studies or other total-body surveys in which functional imaging is performed with radiopharmaceuticals. This will involve customizing the rigid registration and warping algorithms for the specific image type.

Ultimately, considering that an explicit description of the scan type and nature of imaging agent type is available in the image file header, the software could automatically select the appropriate feature detection algorithm based on these parameters, register and correlate different types of images, and possibly provide a composite image incorporating more than one isotope or agent.

APPENDIX

Naming Conventions

We use the following nomenclature for images:

I_o original image, as downloaded from the camera;
I_c cropped image, computed from I_o;
I_e binary eroded image, computed from I_c;
I_r rigidly registered image, computed from I_c;
I_n normalized image, computed from I_r;
I_m matched image, computed from I_n;
I_d differential analysis image, computed from I_m.

In addition, we use the superscript notation to indicate the temporal order of an image in an image sequence, so that I^0, I^1 and I^2 would denote the first, second and third image of the same patient. For the sake of simplicity, we shall refer to the reference image as I^0, although the software allows for any image in the sequence to be taken as reference.

Finally, the pixel count value at coordinates (x, y) of an image I shall be referred to as I(x, y).

REFERENCES

1. Caner B, Kitapcl M, Unlu M, et al. Technetium-99m-MIBI uptake in benign and malignant bone lesions: a comparative study with technetium-99m-MDP. *J Nucl Med* 1992;33:319–324.
2. Ramanna L, Waxman A, Binney G, Waxman S, Mirra J, Rosen G. Thallium-201 scintigraphy in bone sarcoma: comparison with gallium-67 and technetium-MDP in the evaluation of chemotherapeutic response. *J Nucl Med* 1990;31:567–572.
3. Scott A, Kostakoglu L, O'Brien J, Straus D, Abdel-Dayem H, Larson S. Comparison of technetium-99m-MIBI and thallium-201-chloride uptake in primary thyroid lymphoma. *J Nucl Med* 1992;33:1396–1398.
4. Ziegels P, Nocaudie M, Huglo D, et al. Comparison of technetium-99m-methoxyisobutylisonitrile and gallium-67-citrate scanning in the assessment of lymphomas. *Eur J Nucl Med* 1995;22:126–131.
5. Moretti J, Caglar M, Boaziz C, Caillat-Vigneron N, Morere J. Sequential functional imaging with technetium-99m hexakis-2-methoxyisobutylisonitrile and indium-111 octreotide: can we predict the response to chemotherapy in small cell lung cancer? *Eur J Nucl Med* 1995;22:177–180.
6. Aktolun C, Bayhan H, Pabuccu Y, Bilgic H, Acar H, Koylu R. Assessment of tumour necrosis and detection of mediastinal lymph node metastasis in bronchial carcinoma with technetium-99m sestamibi imaging: comparison with CT scan. *Eur J Nucl Med* 1994;21:973–979.
7. Yen T, Lin H, Lee C, Chang S, Yeh S. The role of technetium-99m-sestamibi whole-body scans in diagnosing metastatic Hurtle cell carcinoma of the thyroid gland after total thyroidectomy: a comparison with iodine-131 and thallium-201 whole-body scans. *Eur J Nucl Med* 1994;21:980–983.
8. Scopinaro F, Schillaci O, Scarpini M, et al. Technetium-99m sestamibi: an indicator of breast cancer invasiveness. *Eur J Nucl Med* 1994;21:984–987.
9. Serra J. *Image analysis and mathematical morphology*. London, England: Academic Press; 1982.
10. Ruprecht D, Muller H. Image warping and scattered image interpolation. *IEEE Comp Graph Appl* 1995:37–43.
11. Minoshima S, Berger K, Lee K, Mintun M. An automated method for rotational correction and centering of three-dimensional functional brain images. *J Nucl Med* 1992;33:1579–1585.
12. Minoshima S, Koeppe RA, Frey KA, et al. Anatomic standardization: linear scaling and nonlinear warping of functional brain images. *J Nucl Med* 1994;35:1528–1537.
13. Dann R, Hoford, J, Kovacic S, et al. Evaluation of elastic matching system for anatomic (CT, MR) and functional (PET) cerebral images. *J Comp Assist Tomogr* 1989;13:603–611.
14. Hoh CK, Dahlbom M, Harris G, et al. Automated iterative three-dimensional registration of positron emission tomography images. *J Nucl Med* 1993;34:2009–2018.
15. Alpert N, Bradshaw J, Senda M, Correia J. The principal axis transformation–a method for image registration. *J Nucl Med* 1990;31:1717–1722.
16. Yu J, Fahey F, Gage H, et al. Intermodality, retrospective image registration in the thorax. *J Nucl Med* 1995;36:2333–2338.
17. van den Elsen PA, Pol EJD, Viergever MA. Medical image matching–a review with classification. *IEEE Eng Med Biol* 1993:26–39.
18. Rosenthal MS, Cullom J, Hawkins W, et al. Quantitative SPECT imaging: a review and recommendations by the Focus Committee of the Society of Nuclear Medicine Computer and Instrumentation Council. *J Nucl Med* 1995;36:1489–1513.
19. O'Tuama LA, Treves ST, Larar JN, et al. Thallium-201 versus technetium-99m-MIBI SPECT in evaluation of childhood brain tumors: a within-subject comparison. *J Nucl Med* 1993;34:1045–1051.
20. Packard A, Kronauge J, Limpa-Amara N, Lampson L, O'Tuama L, Jones A. Tumor uptake of ^{99m}Tc-MIBI and ^{201}Tl by a 9L gliosarcoma brain tumor model in rats. *Nucl Med Biol* 1993;20:773–776.
21. Mountz JM, Stafford-Schuck K, McKeever PE, et al. Thallium-201 tumor/cardiac ratio estimation of residual astrocytoma. *J Neurosurg* 1988;68:705–709.
22. Forrest LJ, Dodge RK, Page RL, et al. Relationship between quantitative tumor scintigraphy and time to metastasis in dogs with osteosarcoma. *J Nucl Med* 1992;33:1542–1547.
23. Arad N, Reisfeld D. Image warping using few anchor points and radial functions. *Comput Graph Forum* 1995;14:35–46.
24. Moshfeghi M. Elastic matching of multimodality medical images. CVGIP. *Graph Mod Imag Proc* 1991;53:271–282.